Using Icepack to reproduce Ice Mass Balance buoy observations in landfast ice: improvements from the mushy layer thermodynamics

Mathieu Plante[1], Jean-François Lemieux[1], L. Bruno Tremblay[2], Adrienne Tivy[3], Joey Angnatok[4], François Roy[1], Gregory Smith[1], and Frédéric Dupont[5]

[1]Recherche en prévision numérique environnementale, Environnement et Changement Climatique Canada, Dorval, Québec, Canada.
[2]Department of Atmospheric and Oceanic Sciences, McGill University, Montréal, Québec, Canada
[3]Canadian Ice Service, Environment and Climate Change Canada, Ottawa, Ontario, Canada.
[4]Nunatsiavut Research Center, Nain, Labrador, Canada.
[5]Service Météorologique Canadien, Environnement et Changement Climatique Canada, Dorval, Québec, Canada.

Correspondence: Mathieu Plante (mathieu.plante@ec.gc.ca)

Abstract.

The column thermodynamics package (Icepack v1.1.0) of the Community Ice Code (CICE) version 6 is used to reproduce observations from two Ice Mass Balance (IMB) buoys co-deployed in the landfast ice close to Nain (Labrador) in February 2017. A new automated surface retrieval algorithm is used to determine the ice thickness and snow depths from the measured vertical temperature profiles. The buoys recorded heavy snow precipitation over relatively thin ice, negative ice freeboards and delayed snow flooding. Icepack simulations are produced to evaluate the performance of the Bitz and Lipscomb (1999) thermodynamics used in the Environment and Climate Change Canada (ECCC) ice-ocean systems and to investigate the improvements associated with the use of mushy layer physics. Results show that the Bitz and Lipscomb (1999) scheme produces a smooth thermodynamics growth that fails to capture the observed variability in bottom sea ice congelation rates. The mushy layer physics produces similar temperature profiles but better captures the variability in congelation rates at the ice bottom interface, with periods of rapid ice growth that coincide with IMB observations. Large differences are also found associated with the snow-ice parameterization: the volume of snow-ice formed during flooding is largely underestimated when using a mass conserving snow-formation scheme, but largely improved when using the mushy layer parameterization in which sea-water is filling the porosity of the snow layer. Both schemes are however unable to reproduce the delayed snow-ice formation, as they rely on the hydrostatic balance and do not allow for negative freeboards. This calls for added brine fraction or ice porosity dependencies in the snow-ice parameterizations.

1 Introduction

The sea-ice and oceanography of the Canadian Arctic is largely modulated by the formation of landfast ice in fjords, along the coasts and in narrow channels. For many months each winter, this landfast ice cover inter-connects the land masses of the Canadian Arctic Archipelago (CAA) into a seasonal continent of stationary sea-ice (Melling, 2002; Galley et al., 2012), effectively insulating the sea-water from the cold atmosphere and barring the transport of ice through the CAA passages,

preventing the thick, multi-year ice in the Canada Basin from escaping the central Arctic (Howell et al., 2013; Kwok, 2006). The landfast ice edge represents a seasonal boundary where the air-ocean exchanges and ice dynamics processes are concentrated, in particular by the opening of semi-permanent polynyi under divergent surface forcing conditions (Melling et al., 2001; Dumont

25 et al., 2010). These flaw polynyi in turn drive the regional meteorology (Barber et al., 2001; Gultepe et al., 2003; Lüpkes et al., 2008; Raddatz et al., 2011) and ocean circulation (Dumont et al., 2010), producing sediment-rich waters that are key to the Arctic marine ecosystem (Stirling, 1980, 1997; Carmack and Macdonald, 2002; Tremblay et al., 2002). As changes in the landfast ice cover are expected to alter these processes, its monitoring, representation in forecast models and inclusion in climate projections are a concern not only for the study of the Arctic climate but also for a wide range of socio-economical

30 aspects such as on-ice transport safety, food security and navigation planning (Gearheard et al., 2006; Eicken et al., 2011; Cooley et al., 2020).

In dynamical sea ice models, the physics of landfast ice is represented using a combination of thermodynamic relations governing the ice growth and melt (i.e., a column thermodynamics model, Maykut and Untersteiner, 1971; Semtner, 1976; Bitz and Lipscomb, 1999; Huwald et al., 2005; Turner et al., 2013) and of dynamical parameterizations governing its stabil-

35 ity against external forces (i.e. a rheological model, Hibler, 1979; Hunke and Dukowicz, 1997; Tremblay and Mysak, 1997; Wilchinsky and Feltham, 2004; Rampal et al., 2016). While these components are mostly treated (and developed) independently, they remain deeply inter-connected and the formation of landfast ice usually results from their combined action. In many areas, for instance, the landfast ice is held by the grounding of ice keels on the ocean floor, which involves prior ridging (dynamics) of sufficiently thick ice (thermodynamics). In absence of ice grounding, landfast ice can form during periods of

40 calm and cold weather (Divine et al., 2004; Kirillov et al., 2021) during which leads freeze to a sufficient ice thickness for the unconsolidated ice floes to coalesce together (thermodynamics), allowing the formation of ice arches between pining points that resist subsequent surface forcings (dynamics, Dammann et al., 2019; Liu et al., 2022). In sea ice models, this inter-play between thermodynamic and dynamic factors is represented by ice thickness dependencies in the dynamical parameters, such as the seabed stress term (Lemieux et al., 2015) or the material strength parameters (Dumont et al., 2009; Lemieux et al., 2016;

45 Plante et al., 2020). The accurate representation of landfast ice extent, trends and variability in sea ice models therefore not only requires the permitting dynamics (i.e. ice grounding, tensile strength) but also thermodynamics that reproduces well the landfast ice growth and melt.

In the ECCC ice-ocean forecasting systems (e.g., RIOPSv2, Smith et al., 2021), the implementation of the aforementioned landfast ice dynamics was shown to greatly improve the representation of landfast ice in hindcast (free-run) simulations

50 (Lemieux et al., 2015, 2016). The timings of landfast ice formation and break up however remain difficult to reproduce, often offset by a couple of weeks with respect to those recorded in operation ice charts (Lemieux et al., 2016). While this could be improved by modifications to the ice grounding mechanics (e.g., Dupont et al., 2022) or by changes to the ice strength formulation (Ungermann et al., 2017), it is also possible that the discrepancy is associated with a misrepresentation of the thermodynamics, which in the ECCC systems is based on the model of Bitz and Lipscomb (1999, hereafter BL99). Thermo-

55 dynamics models have grown in sophistication over the years, in particular with the representation of mushy layer physics (Feltham et al., 2006), brine dynamics (Notz and Worster, 2009; Turner et al., 2013) and melt ponds (Flocco et al., 2010; Hol-

land et al., 2012; Hunke et al., 2013). These developments are implemented in the Los Alamos Community Ice CodE version 5 (CICE5) and were shown to increase the overall pan-Arctic ice thickness in both global simulations (Turner and Hunke, 2015) and in coupled climate simulations (in the Community Earth System Model version 2, Bailey et al., 2020). Whether this

60   increase in ice thickness is seen in the landfast ice away from the offshore dynamics remains to be determined.

In recent years, the deployment of Ice Mass Balance (hereafter IMB, used here as a general term, not referring to specific designs) buoys in both the Arctic and Antarctic provided detailed in situ observations of the thermodynamics in the sea ice interior by measuring the internal sea ice temperature at high vertical (centimeters) and temporal (hours) resolution (Richter-Menge et al., 2006; Jackson et al., 2013; Planck et al., 2019). These measurements are made with a thermistor string deployed

65   vertically through the snow and ice layers and provide new insights on the internal transfer of heat that are otherwise not detectable by traditional ice thickness measurements, ice core analysis or remote sensing. The growth and melt of ice is monitored by tracking the vertical position of the material interfaces along the thermistor string, detectable in the temperature profiles due to the different thermal conductivity of air, snow, ice and sea-water (Liao et al., 2019). These thermistor string observations have been used to study the formation of snow ice (Provost et al., 2017; Rösel et al., 2018), to measure the heat

70   fluxes between the material interfaces (West et al., 2020) and to study brine convection and mushy layer properties (Wongpan et al., 2018).

In this study, we assess the performance of the mushy layer thermodynamics with respect to the previous BL99 physics in reproducing the sea ice observations from two IMB buoys deployed in the landfast ice close to Nain (Nunatsiavut), on the Labrador coast. A novel surface retrieval algorithm inspired by the work of Liao et al. (2019) and Cheng et al. (2020) is

75   used to retrieve the ice thickness and snow depths from the internal temperature profiles. The proposed algorithm uses similar assumptions as in Liao et al. (2019) and Cheng et al. (2020) but uses an error minimisation approach to avoid relying on the minimum temperature resolution of the sensors. As in Cheng et al. (2020), it is built to detect snow flooding, which was suspected at our deployment sites in 2017. The IMB buoy observations are then reproduced using Icepackv1.1.0, the column thermodynamics package of CICE version 6, used here as a column thermodynamics model. This analysis is part of an effort

80   to assess the benefits of upgrading the sea ice model component from CICE4 to CICE6 in the ECCC forecast systems.

This manuscript is organised as follows. The Icepack1.1.0 model physics is briefly described in section 2, with the two schemes used in the analysis (BL99 and mushy layer physics). The methods are detailed in section 3, including the buoy deployments, the surface retrieval algorithm and the simulations setup. Results from the thermistor string observations and Icepackv1.1.0 simulations are presented in section 4, and a discussion on the model performance is provided in section 5.

85   Conclusions are summarized in section 6.

2   Icepack v1.1.0 thermodynamics

2.1   Surface thermodynamic balance

The thermodynamic growth and melt of sea ice are governed by the net energy balance at the top and bottom ice (or snow) surfaces. The net heat flux F_0 (positive downward) at the top interface is written as:

$$F_0 = F_s + F_l + F_{LW} + (1 - \alpha)(1 - i_0)F_{SW} \tag{1}$$

where F_s is the sensible heat flux, F_l is the latent heat flux, F_{LW} is the net long wave flux, α is the surface shortwave albedo, i_0 is the fraction of short wave penetration into the ice or snow surface and F_{SW} is the incoming shortwave flux. In all simulations, the shortwave albedo and penetration are defined by the Community Climate System Model version 3 (CCSM3, Collins et al., 2006) radiation scheme, and the atmospheric fluxes are taken from the ECCC Global Deterministic Prediction System (GDPS, Buehner et al., 2015; Smith et al., 2018) at the grid point location closest to the buoy deployment.

The amount of ice or snow melt at the top interface is given by the imbalance between the net heat flux (F_0) and the conductive heat flux (F_{ct}) from the ice below. That is:

$$-q(T,S)\frac{\partial h}{\partial t} = \begin{cases} F_0 - F_{ct} & \text{if } F_0 > F_{ct} \\ 0 & \text{otherwise} \end{cases} \tag{2}$$

where $q(T,S)$ is the enthalpy of snow or ice at the top surface, T and S are the ice temperature and salinity, and h is the ice (or snow) thickness.

At the ice base, the thermodynamic balance is computed using the Icepack v1.1.0 ocean mixed layer parameterization. The net heat exchange F_{bot} at the ice-ocean interface is given by:

$$F_{bot} = -\rho_w c_w c_h u_*(T_w - T_f), \tag{3}$$

where ρ_w (= 1026 kg/m^3) is the sea water density, c_w is the sea water specific heat capacity (= 4.218 kJ kg^{-1} K^{-1}), c_h (= 0.006) is a heat transfer coefficient, u_* is the ocean friction velocity (set here to 0.005 m s^{-1}) and T_w, T_f are the sea surface and bottom ice surface temperatures respectively.

The amount of ice congelation or melt at the ice bottom is given by the imbalance between F_{bot} and the conductive heat flux (F_{ct}) from the ice interior, according to:

$$q(T,S)\frac{\partial h}{\partial t} = (F_{bot} - F_{cb}), \tag{4}$$

where q is the enthalpy at the ice bottom interface and F_{cb} is the conductive flux at the ice-ocean interface.

2.2 Vertical T, S and q profiles

2.2.1 BL99 physics

In the BL99 physics, sea ice is treated as a single phased solid but the effect of brine on the thermodynamics is included via salinity dependencies in the heat conductivity and specific capacity definitions. The salinity in each ice layers is fixed and based on observed vertical salinity profiles (see Bitz and Lipscomb, 1999, for details).

The evolution of the vertical temperature profile in this scheme is given by:

$$\rho_i c_i \frac{\partial T_i}{\partial t} = \frac{\partial}{\partial z}\Big(K_i \frac{\partial T_i}{\partial z}\Big) - \frac{\partial}{\partial z}\big(I_{pen}(z)\big), \tag{5}$$

where ρ_i is the ice or snow density ($= 917$ kg/m^3 for sea ice, $\rho_s = 330$ kg/m^3 for snow), $c_i(T,S)$ is the specific heat of sea ice or snow, T_i is the internal temperature in the ice or snow layer, K_i is the thermal conductivity based on the Bubbly parameterization (Pringle et al., 2007), and $I_{pen}(z)$ is the flux of penetrating solar radiation at depth z according to Beer's law. The vertical temperature profile is solved with $F_0 = F_{ct}$ serving as boundary condition at the top surface (if $T_{air} < 0$); otherwise the surface temperature T_{sf} is set to 0°C. The bottom boundary condition is equal to the salinity-dependent freezing point temperature of sea-water.

Finally, the enthalpy $q(T,S)$ at the top surface (in Eq. 2), the ice base (in 3) and in each snow or ice layer are calculated from the solved temperatures, as follows:

$$q(T,S) = -\rho\Big[c_0(T_m - T) + L_0\big(1 - \frac{T_m}{T}\big) - c_w T_m\Big], \tag{6}$$

where S is the sea ice bulk salinity, c_0 is the specific heat of fresh ice at 0°, $T_m(S)$ is the melting temperature of sea ice as determined by a salinity-dependent liquidus relation, L_0 is the latent heat of fusion of fresh ice at 0° and c_w is the specific heat capacity of brine.

2.2.2 Mushy layer physics

In the mushy layer thermodynamics, sea ice is assumed to be a mixed-phase layer composed of both pure ice and liquid brine inclusions, with proportions that are determined by prognostic temperature and salinity relations (Feltham et al., 2006; Turner et al., 2013). The evolution of the temperature in the mushy layers is governed by a prognostic equation for enthalpy:

$$\frac{\partial q}{\partial t} = \frac{\partial}{\partial z}\Big(K_i \frac{\partial T_i}{\partial z}\Big) + w\frac{\partial q_{br}}{\partial z} - \frac{\partial}{\partial z}\big(I_{pen}(z)\big), \tag{7}$$

where q_{br} is the enthalpy of the brine and w is the Darcy velocity of the brine. The enthalpy q is defined in terms of the brine fraction and temperature, as:

$$
\begin{aligned}
q &= \phi q_{br} + (1-\phi)q_i \\
&= \phi \rho_w c_w T + (1-\phi)(\rho_i c_i T - \rho_i L_0)
\end{aligned} \tag{8}
$$

where q_i is the enthalpy of fresh ice and ϕ is the brine fraction defined as:

$$\phi = \frac{S}{S_{br}}, \tag{9}$$

140   where S_{br} the salinity of the brine as defined by an observation-based liquidus relation (Turner et al., 2013). Together, equations 7 and 8 differ from the BL99 thermodynamics only from the additional heat advection from brine flow and the mixed-phase enthalpy definition.

    The prognostic equation for the internal salinity includes dependencies on brine processes such as gravity drainage and melt pond flushing (Notz and Worster, 2009; Turner et al., 2013). The salinity equation is written as:

145    $$\frac{\partial S}{\partial t} = w\frac{\partial S_{br}}{\partial z} + G, \tag{10}$$

where G is a source term representing the slow mode of brine drainage. The reader is referred to Turner et al. (2013) for more details.

2.3 Snow-ice formation

The BL99 and the mushy layer physics include a snow-ice parameterization to represent the growth of ice associated with snow
150   flooding and it subsequent (but here assumed instantaneous) refreezing on top of the ice surface. Both schemes use the same hydrostatic equilibrium equation to determine whenever the snow weight brings the ice surface below the water line, but differ in the method at which snow is being converted to sea ice.

    The threshold for snow-ice formation is based on Archimedes law:

$$h_s > \frac{(\rho_w - \rho_i)h_i}{\rho_s}, \tag{11}$$

155   where h_s is the snow depth. In the BL99 scheme, the change in snow and ice thicknesses ($\delta h_s, \delta h_i$) associated with snow-ice formation is governed by a mass-conserving scheme:

$$\delta h_s = \frac{-\rho_i h^*}{\rho_w}, \tag{12}$$

$$\delta h_i = \frac{\rho_s h^*}{\rho_w}, \tag{13}$$

160   where h^* is the amount of snow in excess of the hydrostatic equilibrium thickness before the snow-ice conversion. In the mushy layer scheme, it is assumed instead that sea-water is advected laterally or percolates through the ice layer, adding mass by filling the porosity of the snow layer. The change in snow and ice thicknesses are given by:

$$\delta h_i = -\delta h_s = \frac{m_{fb}}{\rho_w - \rho_s + \rho_{snice}}, \tag{14}$$

where m_{fb} ($= h_i\rho_i + h_s\rho_s - h_i\rho_w$) is the combined mass of snow and ice in excess of the hydrostatic equilibrium prior to the
165   snow-ice formation and ρ_{snice} is the density of the newly formed snow-ice. The snow-ice density and liquid fraction ϕ_{snice}

are defined by assuming that sea-water has filled the porosity of the snow-layer:

$$\phi_{snice} = 1 - \rho_s/\rho_i, \tag{15}$$

$$\rho_{snice} = \rho_w \phi_{snice} + \rho_i(1 - \phi_{snice}). \tag{16}$$

3 Methods

The BL99 and mushy layer physics are tested against in situ observations by running Icepack v1.1.0 simulations with each physical scheme to reproduce data records from two IMB buoys deployed in the landfast ice. All simulations use 7 ice layers, 1 snow layer and are initialized using the ice thickness, snow depth and internal ice temperature (interpolated into 7+1 layers) recorded by the buoys a few days after their deployment. The simulations are ran until early summer (June 4th), well past the buoy recovery date, with a time-step of 3 hours.

3.1 IMB buoy deployments

Two IMB buoys from the Scottish Association for Marine Science (SAMS) were deployed in winter 2017 as part of an ongoing collaboration with the Nunatsiavut Research Center (NRC) with the goal of serving the Nain community with the deployment of scientific instruments in the local landfast ice. The deployment locations were chosen with NRC collaborators based on community needs. The first buoy (IMB1) was deployed on February 23rd, 2017 at $\sim56.42°$ N, $61.7°$ W, in a landfast channel close to the southern coast of Satosoak island (see Fig. 1), and recovered two months later on April 18th. The second buoy (IMB2) was deployed during the same field season on February 24th at $\sim56.43°$ N, $61.50°$W, ~ 10 km East of IMB1 in the same fjord close to Palungitak island, and recovered three months later on May 31st.

The SAMS IMB buoys consist of a 5 m long thermistor string with temperature sensors (Maxim DS28EA00, with $0.0625°$C resolution and $0.0625°$C accuracy) placed every 2 centimeters (Jackson et al., 2013). The thermistor strings are deployed vertically through a 5-cm hole such that the sensors measure the vertical temperature profile from the atmosphere above the snow layer down to the sea-water below the ice (Fig. 2a). At deployment, a section of the thermistor string is laid flat on the ice surface to mark the initial snow/ice interface in the data (see red arrows and dashed lines in Fig. 2a-b). The sensors within this thermistor string section are thus all at the same depth and show nearly identical temperature readings, making this segment easily identifiable in the vertical temperature profiles. The hole is then refilled with slush, the snow cover is carefully restored to its original depth. The vertical temperature profiles are measured with a 6-hour time resolution and are transmitted remotely via Iridium satellite with the air temperature, atmospheric pressure and GPS location. The SAMS buoys also perform daily heat cycle measurements, which consist in recording the temperature change associated with a one- and two-minute heating from a resistor component besides each temperature sensor (Jackson et al., 2013). This change in temperature can be used to infer the heat capacity of the medium surrounding the sensors.

3.2 Automated surface retrieval algorithm

A new automated surface retrieval algorithm is used to identify three material interfaces from the IMB temperature profiles (the top of the snow layer, the snow/ice interface and the ice bottom, see Fig. 2). Since a segment of the thermistor string is laid flat (horizontal) on the ice surface at deployment, the algorithm also needs to identify the first and last sensors of this "thermistor plateau", which ends up being embedded into the ice after flooding events (see Fig. 2b for in the flooded ice case). This result in 5 sensor positions to be identified.

The surface retrieval algorithm is based on the following assumptions:

1. The temperature profiles are piece-wise linear.

2. The ice surface does not move below its original position along the thermistor string after deployment (i.e., no vertical slip between the buoys and the ice, and no surface melting).

3. The minimum temperature along the thermistor string is located above the snow layer.

4. The vertical profiles are isothermal in the atmosphere and in the ocean.

These assumptions are similar to those from Liao et al. (2019); Zuo et al. (2018); Cheng et al. (2020), and relate to the dependency of the algorithm on the difference in heat conductivity (i.e. vertical temperature gradient) in the snow and ice layers. Heat-conductivity based surface retrieval algorithms are thus, by construction, not suited for isothermal conditions (e.g. during thaw), in which case other observations (e.g. from sonar data or heat cycles) are needed to determine the ice mass balance. The algorithm described below is similar to that of Cheng et al. (2020) but differs in the detection criteria for each interface.

3.2.1 Temperature gradient and curvature

The vertical temperature gradient β and curvature γ are first calculated at each sensor location and for the entire data record using a centered finite difference scheme. The vertical temperature gradient at the kth sensor location is defined as:

$$\beta_k = \frac{\partial T_k}{\partial z} \sim \frac{T_{k+1} - T_{k-1}}{2\Delta z}. \tag{17}$$

where T_k represent the temperature reading of the kth sensor and Δz is the spacing between two sensors (here 2 cm). The temperature profile curvature at point k is defined as:

$$\gamma_k = \frac{\partial^2 T_k}{\partial z^2} \sim \frac{T_{k+1} - 2T_k + T_{k-1}}{\Delta z^2}. \tag{18}$$

3.2.2 Initial ice surface and thermistor plateau

For each buoy, the thermistor plateau is set at deployment and remains fixed over the entire record. The initial ice surface Z_{ice0} (with temperature T_{ice0}) and lower end of the thermistor plateau serve as reference points for the algorithm.

The position Z_{ice0} is identified by the minimum curvature ($\min(\gamma_k)$) below the maximum vertical temperature gradient in
225   the profiles (assumed to be inside the snow layer, Fig. 2). The other end of the thermistor plateau Z_p is identified by the closest
local maxima in curvature below Z_{ice0}. To remove sensitivity to sporadic variations in the detected interfaces ($\pm 2cm$), the
reference locations are defined as the statistical mode of Z_{ice0} and Z_p over the first 7 days of records.

3.2.3   Ice-ocean interface

For each profile, the position of the ice basal interface is determined using a minimization approach to find the location of
230   the corresponding temperature inflection. That is, each sensor location in the vicinity of the ice bottom is associated with a
theoretical piece-wise linear temperature profile, set as:

$$T_k^{th} = \begin{cases} T_c + (z_k - Z_c)\beta_{ice} & Z_c > z_k > Z_{bot} \\ T_w & z_k < Z_{bot} \end{cases} \tag{19}$$

where T_k^{th} is the theoretical temperature at sensor location z_k, T_c is the temperature observed at a position Z_c in the ice interior,
(i.e. $T_c \sim T_w + r(T_{ice0} - T_w)$, where $r = 1/3$ is an arbitrary ratio), β_{ice} is an ice temperature gradient approximation, Z_{bot} is
235   the position of the ice-ocean interface and T_w is the observed ocean temperature. The gradient β_{ice} for each theoretical profile
is approximated as:

$$\beta_{ice} = \frac{T_w - T_c}{Z_{bot} - Z_c}, \tag{20}$$

The ice bottom interface Z_{i-o} is then defined as the position Z_{bot} from the theoretical profile that minimizes the following
error function:

240   $$err = \sum_{k=0}^{N} (T_k^{th} - T_k^{obs})^2. \tag{21}$$

where T_k^{obs} is the observed temperature at sensor position k.

Note that this detection method differs significantly from the temperature selection method of Liao et al. (2019) and Cheng
et al. (2020), and has the benefit of not depending on the sensor type and precision.

3.2.4   Air-snow interface

245   The air-snow interface position Z_{a-s} is found by identifying the maximum vertical temperature curvature γ_k below the sensor
with the coldest temperature (assumed to be in the air) and above the initial ice surface Z_{ice0}. The temperature gradient directly
below Z_{ice0} must also be smaller than a threshold for snow detection, set at $0.1\,^\circ\mathrm{C}\,\mathrm{cm}^{-1}$. Note that this threshold is significantly
smaller than in Liao et al. (2019) but is only used to discriminate curvatures associated with noise in the data.

The temperature gradient in the snow layer is then defined as:

250   $$\beta_{snow} = \frac{T_{ice0} - T_{a-s}}{Z_{ice0} - Z_{a-s}}, \tag{22}$$

where T_{a-s} is the temperature reading at Z_{a-s}.

3.2.5 Snow-ice interface

The presence of snow-ice above the initial ice surface is detected by comparing the temperature gradient directly above the initial ice surface Z_{ice0} with that in the snow layer and in the ice below. That is, sensors above the original ice surface are associated with snow-ice if the local temperature gradient satisfies:

$$\beta_k < \beta_{ice} + r_{si}(\beta_{snow} - \beta ice). \tag{23}$$

where r_{si} ($= 1/5$) is a ratio between 0 and 1. If such a gradient is present above Z_{ice0}, the new ice surface position (Z_{s-i}) is set as the lowest point where $\beta_k < \beta_{si}$.

Note that while arbitrary, the ratio r_{si} for snow-ice detection ensures that the snow-ice conductivity is closer to that of sea-ice, while filtering fluctuations due to changing temperature conditions. The snow-ice detection is the only component of the algorithm that depends on the other detected interfaces.

3.2.6 Ice thickness, snow depth and free-board

The ice thickness h_i (including snow-ice), snow depth h_s and snow-ice thickness h_{si} are calculated from the detected interfaces, according to:

$$h_i = Z_p - Z_{bot} + Z_{s-i} - Z_{ice0}, \tag{24}$$

$$h_s = Z_{a-s} - Z_{s-i}, \tag{25}$$

$$h_{si} = Z_{s-i} - Z_{ice0}. \tag{26}$$

The ice freeboard h_{fb} (the elevation of the snow-ice interface above the water line) can then be found based on the hydrostatic balance:

$$h_{fb} = h_i - \frac{\rho_s h_s + \rho_i h_i}{\rho_w}. \tag{27}$$

with densities set to their respective Icepack values (see section 2). The freeboard measurements have a precision of ~ 1.0 cm, based on the propagation of uncertainty and assuming an error of 2 cm for the snow/ice thicknesses and of 33 kg m^3 for the snow density (King et al., 2020). Note that a negative freeboard value indicates that the snow-ice interface is below the water line, with the ice in hydrostatic imbalance.

3.2.7 Basal conductive flux

Lastly, the conductive fluxes F_{cb} at the ice bottom is approximated based on the method of West et al. (2020), using:

$$F_{cb} \sim K_i \frac{\partial T}{\partial z}. \tag{28}$$

where K_i is the ice thermal conductivity (defined here using the Bubbly parameterization and the temperature recorded at Z_{ice0}, Pringle et al., 2007) and where the temperature gradient is obtained from the temperature profile in the layer 20-50 cm above the detected ice-ocean interface.

4 Results

4.1 Surface retrieval algorithm validation

The surface retrieval algorithm successfully identifies the snow and ice interfaces in most of the records (Fig 3). The algorithm fails during two warm spells (on March 9-11 and April 6-10, Fig 3b-c) when a negligible vertical temperature gradients or

285 temperature inversions is present within the snow and ice layers (i.e. the piece-wise linear assumption does not hold). The surface retrieval algorithm is also generally not successful during the melt season (beyond April 16th) for the same reason, except on occasional colder days.

The detected snow interfaces correspond well with the layer where large vertical temperature gradients are present (Fig. 4) and most of the variability associated with diurnal cycles or synoptic systems are damped (see warming and cooling rates in

290 Fig. 5). The upward migrations of the detected snow-ice interface during flooding correspond well with the warm temperatures recorded above the initial ice surface. In particular, the onset of flooding at IMB2 (on March 26th) coincides with a sudden warming event at the snow-ice interface that propagates upward in the snow layer despite cooling temperatures in the air above (indicated by the purple arrow in Fig. 5b). This signal is expected in the case of snow flooding due to upward percolation or lateral advection of sea-water (Provost et al., 2017). On the other hand, flooding at the IMB1 site is only detected late in

295 the observational record (on April 25th) when temperatures above freezing are reached regularly. It is not associated with a warming signal, and could result from liquid precipitation or surface melting.

The top and bottom ice interfaces show good agreement with the warming of sensors recorded during the heating cycles (Fig. 6). The detected air-snow interface position is also coherent with the section measuring the largest warming, although this is more difficult to assess with certainty because of variations in the recorded warming in and above the snow layers, which we

300 attribute to variations in snow density. Note that the IMB2 warming records (Fig. 6b) do not show a sharp snow-ice interface but rather a smooth vertical gradient over 2-4 cm within the thermistor plateau. This indicates a ($\sim$1-2 cm) thickness uncertainty related to the marking of the initial ice surface with the thermistor plateau, which we speculate was not exactly horizontal on the snow-ice interface. This positional uncertainty remains for the entire record, even though the warming gradient disappears after the thermistor plateau is flooded.

305 4.2 In situ ice mass balance conditions

From the beginning of the observational records, the IMB buoys present large snow depths ($\sim$20-40 cm) over relatively thin ice ($\sim$75-100 cm) such that the measured freeboard occasionally dips to negative values (Fig. 7a). Both sites present similar snow-depth variations, with significant increases during each warm events and subsequent decreases likely resulting from snow compaction and redistribution by the winds. The snow depths are generally larger at the IMB2 site (by $\sim$ 5-10 cm), with a large

310 but short-lived maxima of 50 cm likely resulting from snow accretion and subsequent removal by the winds around the buoy.

The local ice mass balance at the two sites is largely influenced by the snow layer. The thinner snow cover (i.e. lesser insulation) at the IMB1 site results in colder internal ice temperatures, larger congelation rates and smaller amounts of snow flooding (Fig. 7b). With an initial ice thickness and snow depth of 80 cm and 22 cm respectively (on March 1st), the IMB1

freeboard reach negative values after each snow fall event, to -1.1 cm on March 16th and -1.6 cm on April 14th. Snow flooding
315 is only detected from April 25th onward. The ice thickness reached its detected maximum (100 cm) on May 1st, representing
a total ice thickness increase of 20 cm from which 16 cm is associated with congelation at the ice-ocean interface and 4 cm
is associated with snow-ice formation. In comparison, the IMB2 buoy initially recorded a 28 cm snow depth and 76 cm ice
thickness (on March 1st), for a freeboard of -1.6 cm. Snow falls during the first warm event brought the freeboard to a minimum
of -4.3 cm on March 16th, and snow flooding detected from March 26th onward. The flooding of the snow layer at the IMB2
320 site coincide with a large (14 cm) reduction in the snow depth and is the main contributor to the ice mass balance. By April
6th, the ice thickness reached a maximum of 98 cm for a total ice growth of 22 cm, 14 cm of which is attributed to snow-ice
formation and 8 cm to congelation.

4.3 Icepack simulations

The Icepack simulations capture well the overall sea ice growth of $\sim$20 cm during the observation period but generally fails to
325 reproduce the observed variability in both ice thickness and snow depths (Fig. 8). The lack of snow depth variability is partly
attributed to the simple snow model used in the simulations, which does not account for snow compaction and redistribution, but
mostly to the hydrostatic-based snow-ice formation scheme: with initialized snow depths close to or exceeding the hydrostatic
balance, any subsequent snow precipitation is immediately transformed into snow-ice (Fig. 8c-d for freeboard values and Fig.
9c-d for snow-ice volumes). The conversion of snow to snow-ice at each snow-fall event in turn produces rapid increases in ice
330 thickness that deviate from observations, and leads to an overestimation of the ice thickness early in the simulations.

The error in snow-ice formation is larger in the mushy simulations compared to BL99 (Fig. 9c-d). This is due to the mass-
conserving snow-ice parameterization in the BL99 simulations, which largely underestimates the volume of the transformed
snow-ice (a cumulative 2.2 and 5.3 cm for the IMB1 and IMB2 simulations respectively, compared to 4 and 14 cm in the
buoy observations). This leads to an underestimation of the ice thickness at the end of the simulations, especially in the IMB2
335 site where the snow-ice is a major contributor to the observed ice mass balance (see Fig. 9b,d). The volume of snow-ice is
largely improved when using the mushy layer physics, with 8 and 16 cm in the IMB1 and IMB2 simulations respectively. Note
however that while this leads to a better agreement with observations after the observed snow flooding onset, it worsens the ice
thickness discrepancy early in the mushy simulations (Fig. 9d).

In terms of ice congelation, the BL99 simulations show smooth and steady growth rates (~ 0.3 cm day^{-1}, decreasing
340 towards spring) with little short-term variability (Fig. 9a-b). This differs significantly from the observations, in which most
of the congelation occurs in short periods of rapid ice growth, and indicates an insufficient sensitivity to the atmospheric
conditions and synoptic-scale forcing. This discrepancy is significantly improved in the mushy layer simulations, in which the
periods of rapid ice growth are well reproduced (see green lines in Fig 9a-b). This improvement is not attributed to differences
in internal temperature or conductive heat fluxes, but rather to the consideration of the liquid fraction when computing the
345 sea ice enthalpy at a given ice temperature, affecting the energy balance at the ice-ocean interface. This is demonstrated by
repeating the simulations without the snow-ice parameterizations, in which case both the BL99 and mushy layer simulations

presents nearly identical conductive fluxes in the lowest ice layer but presents the same differences in ice congelation rates (Fig. 10 for the IMB1 simulations).

Note that removing the snow-ice parameterization from the simulations results in larger and more variable snow depths in the Icepack simulations. This effectively removes the largest source of discrepancy with the observations up to the flooding onset (Fig .10a), but leads to an underestimation of the ice thickness by the end of the simulations due to the missing snow-ice contribution to the ice mass balance. Note also that while the increased insulation results in smaller congelation rates in the BL99 simulations, the absence of flooding yields larger congelation rates in the mushy layer simulations (Fig. 11 for the IMB2 simulations). This difference is attributed to the mushy layer physics that represents the warming from the added liquid water content when flooding, which increases the brine fraction, warms the ice interior and suppresses bottom ice congelation. Removing the flooding thus results in a colder ice in the mushy layer simulations, despite the increased insulation from the thicker snow layer.

5 Discussion

The in situ observations presented in this analysis are in line with a number of negative freeboard measurements reported in recent years in the Arctic (Rösel et al., 2018; Provost et al., 2017), which are likely to become more frequent as the sea ice thins and precipitation increases in the transition to a seasonal ice cover (Merkouriadi et al., 2020). It remains however that snow flooding is relatively infrequent: these in situ snow flooding observations were associated with anomalous 2017 snow conditions that have not yet re-occured in subsequent (2018-2022) landfast ice observation campaigns. The frequency at which the snow flooding contributes to the ice mass balance in landfast ice areas, in Nain but also more widely along the Canadian coastlines and in the Canadian Arctic Archipelago, remains to be determined. Note however that snow-ice formation is more likely a significant contributor to the ice mass balance over thin ice (Granskog et al., 2017), and is thus more likely to occur earlier in the growth season. The earlier ice growth could be better assessed with IMB buoys deployed in open water prior to the freeze-up. Such a deployment was attempted in 2022 in Nain, but buoy icing, floe drifting and wave battering prevented the measurement of a continuous time series during the freeze-up period.

The large discrepancies between the observed and simulated snow flooding onset in the analysis demonstrates that the hydrostatic-based snow-ice parameterizations are not able to capture the more complex processes usually described from in situ flooding observations, which often include additional porosity conditions for the percolation of sea-water through the brine channels (Eicken et al., 1995; Maksym and Jeffries, 2000) or dynamical processes such as lateral advection from neighbouring sites of sea ice deformation (Provost et al., 2017). One advantage of the mushy layer thermodynamics is that it contains all the necessary ingredients for porosity conditions (permeability, liquid fraction, Darcy velocity) to be added for the snow flooding onset. For instance, adding a simple minimum porosity criterion to the snow-ice parameterization in the IMB2 simulation effectively improves the simulations by delaying the snow-ice formation by several weeks (Fig. 12). Note however that in this simple experiment, the snow-ice conversion remains hydrostatic-based such that a large volume of snow-ice is instantaneously formed once the delayed flooding occurs. Further modifications are thus necessary to adequately

380 reproduce the slower flooding recorded at the IMB2 site, such as a snow-conversion function of the Darcy velocity. The instantaneous flooding could nevertheless represent flooding by lateral advection of sea-water. Defining dynamical thresholds for this processes to happen is likely more involved as it requires a form of coupling between the snow-ice parameterization and the dynamical (or thermal stressing) components of the sea ice model.

The results presented show that the inclusion of brine processes in the mushy layer thermodynamics yields an increased

385 sensitivity to external forcing and physical processes that are likely to positively affect the landfast ice dynamics. For instance, the larger congelation rates simulated under colder air conditions may allow for faster sea ice consolidation (increasing the effective ice strength) and ease the formation of ice arches in narrow passages. On the other hand, the consideration of the heat transfer from brine advection allows a warming of the ice interior in association with any added liquid content (e.g. from flooding, precipitation or surface melt), likely impacting the ice strength heterogeneity (especially when using an ice

390 thickness distribution) early in the thaw season which could affect the timing and variability of landfast ice break up. The mushy layer thermodynamics thus presents itself as a useful, if not necessary, step towards improving the coupling between the thermodynamic and dynamics sea ice model components.

6 Conclusions

The thermodynamic growth of landfast ice in the vicinity of Nain (Labrador) is investigated from two Ice Mass Balance (IMB)

395 buoys from the Scottish Association for Marine Science (SAMS) deployed in winter 2017. The observed thermodynamics are reproduced using Icepack v1.1.0, the column thermodynamics package of the Community Ice Code (CICE) version 6, with two different physical schemes: the Bitz and Lipscomb (1999) physics that represents the thermodynamics currently used in the Environment and Climate Change Canada (ECCC) ice-ocean forecasting systems, and the mushy layer thermodynamics (Feltham et al., 2006; Notz and Worster, 2009; Turner et al., 2013) that includes new physics available in CICE6. The perfor-

400 mance of Icepack in reproducing the IMB observations is assessed with a particular attention to the improvements associated with the use of the mushy layer physics.

A new automated surface retrieval algorithm is used to infer the evolution of the ice and snow thicknesses from the IMB temperature records. The algorithm is similar to those introduced by Liao et al. (2019) and Cheng et al. (2020) but uses different detection criteria to avoid relying on the minimum temperature resolution of the sensors. The detected air-snow, snow-ice and

405 ice-ocean interface positions are in good agreement with the interfaces seen in the vertical temperature gradients and in heat cycle measurements. The algorithm adequately detects snow flooding events at each sites by allowing an upward migration of the snow-ice interface.

The IMB observations in winter 2017 are characterized by thick snow over relatively thin ice, resulting in negative ice freeboard values for several days until delayed snow flooding events occur. The large variations in snow depth at the two

410 sites is a major driver of the sea ice mass balance and demonstrates the importance of adequately capturing snow processes (redistribution, compaction, snow-ice formation) in sea ice models. In particular, the different snow depth at the two locations lead to different contributions of snow-ice formation and ice congelation in the ice mass balance: the IMB1 site with deeper

snow depths shows warmer ice temperatures, weaker congelation rates and earlier and more voluminous snow flooding, while the growth at the IMB2 site is mostly driven by ice congelation.

415   The Icepack simulations reproduce well the overall ∼20 cm landfast ice growth during the observation period but has difficulties in reproducing the snow processes. In particular, the inability of the model to produce negative freeboards leads to erroneous snow-ice formation onsets. Any subsequent snow precipitation are instantly converted to ice, effectively locking the snow depth to a ratio of the snow/ice thicknesses for the remaining of the simulations. This effect is also seen in the mushy layer simulations, but with improved (larger) snow-ice volume. The consideration of liquid fraction in the mushy layer

420   simulations effectively adds missing sensitivities in the BL99 thermodynamics: it better reproduce the observed periods of rapid ice congelation and represents the ice interior warming associated with flooding. This is likely to affect the representation of landfast ice by allowing for faster sea ice consolidation and for added variability in the early melt season, but this needs be assessed in future work.

Code and data availability.   All codes (model and analysis) are available on github upon request. The buoy data are available upon request.

425   *Author contributions.*   MP implemented Icepack v1.1.0 as a column model and produced the simulations with assistance from JFL, FR and FD. AT and JA deployed the ice mass balance buoys. MP coded the surface retrieval algorithm with contributions from GS. MP, JFL, BT, FR, FD and GS analysed and discussed the results. MP wrote the manuscript with edits from JFL, BT, FR, GS, AT and FD.

Competing interests.   The authors declare that they have no conflict of interest.

Acknowledgements.   We thank the Nunatsiavut Research Center for assistance and support for the ice mass balance buoy deployment and
430   retrieval.

References

Bailey, D. A., Holland, M. M., DuVivier, A. K., Hunke, E. C., and Turner, A. K.: Impact of a New Sea Ice Thermodynamic Formulation in the CESM2 Sea Ice Component, Journal of Advances in Modeling Earth Systems, 12, e2020MS002 154, https://doi.org/https://doi.org/10.1029/2020MS002154, e2020MS002154 2020MS002154, 2020.

435 Barber, D., Hanesiak, J., Chan, W., and Piwowar, J.: Sea-ice and meteorological conditions in Northern Baffin Bay and the North Water polynya between 1979 and 1996, Atmosphere-Ocean, 39, 343–359, https://doi.org/10.1080/07055900.2001.9649685, 2001.

Bitz, C. M. and Lipscomb, W. H.: An energy-conserving thermodynamic model of sea ice, Journal of Geophysical Research: Oceans, 104, 15 669–15 677, https://doi.org/10.1029/1999JC900100, 1999.

Buehner, M., McTaggart-Cowan, R., Beaulne, A., Charette, C., Garand, L., Heilliette, S., Lapalme, E., Laroche, S., Macpherson, S. R.,
440 Morneau, J., and Zadra, A.: Implementation of Deterministic Weather Forecasting Systems Based on Ensemble–Variational Data Assimilation at Environment Canada. Part I: The Global System, Monthly Weather Review, 143, 2532 – 2559, https://doi.org/10.1175/MWR-D-14-00354.1, 2015.

Carmack, E. C. and Macdonald, R.: Oceanography of the Canadian Shelf of the Beaufort Sea: A Setting for Marine Life, Arctic, 55, 29–45, 2002.

445 Cheng, Y., Cheng, B., Zheng, F., Vihma, T., Kontu, A., Yang, Q., and Liao, Z.: Air/snow, snow/ice and ice/water interfaces detection from high-resolution vertical temperature profiles measured by ice mass-balance buoys on an Arctic lake, Annals of Glaciology, 61, 309–319, https://doi.org/10.1017/aog.2020.51, 2020.

Collins, W. D., Bitz, C. M., Blackmon, M. L., Bonan, G. B., Bretherton, C. S., Carton, J. A., Chang, P., Doney, S. C., Hack, J. J., Henderson, T. B., Kiehl, J. T., Large, W. G., McKenna, D. S., Santer, B. D., and Smith, R. D.: The Community Climate System Model Version 3
450 (CCSM3), Journal of Climate, 19, 2122 – 2143, https://doi.org/10.1175/JCLI3761.1, 2006.

Cooley, S. W., Ryan, J. C., Smith, L. C., Horvat, C., Pearson, B., Dale, B., and Lynch, A. H.: Coldest Canadian Arctic communities face greatest reductions in shorefast sea ice, Nature Climate Change, 10, 533–538, https://doi.org/10.1038/s41558-020-0757-5, 2020.

Dammann, D. O., Eriksson, L. E. B., Mahoney, A. R., Eicken, H., and Meyer, F. J.: Mapping pan-Arctic landfast sea ice stability using Sentinel-1 interferometry, The Cryosphere, 13, 557–577, https://doi.org/10.5194/tc-13-557-2019, 2019.

455 Divine, D. V., Korsnes, R., and Makshtas, A. P.: Temporal and spatial variation of shore-fast ice in the Kara Sea, Continental Shelf Research, 24, 1717–1736, https://doi.org/https://doi.org/10.1016/j.csr.2004.05.010, 2004.

Dumont, D., Gratton, Y., and Arbetter, T. E.: Modeling the Dynamics of the North Water Polynya Ice Bridge, Journal of Physical Oceanography, 39, 1448 – 1461, https://doi.org/10.1175/2008JPO3965.1, 2009.

Dumont, D., Gratton, Y., and Arbetter, T. E.: Modeling Wind-Driven Circulation and Landfast Ice-Edge Processes during Polynya Events in
460 Northern Baffin Bay, Journal of Physical Oceanography, 40, 1356 – 1372, https://doi.org/10.1175/2010JPO4292.1, 2010.

Dupont, F., Dumont, D., Lemieux, J.-F., Dumas-Lefebvre, E., and Caya, A.: A probabilistic seabed–ice keel interaction model, The Cryosphere, 16, 1963–1977, https://doi.org/10.5194/tc-16-1963-2022, 2022.

Eicken, H., Fischer, H., and Lemke, P.: Effects of the snow cover on Antarctic sea ice and potential modulation of its response to climate change, Annals of Glaciology, 21, 369–376, https://doi.org/10.3189/S0260305500016086, 1995.

465 Eicken, H., Jones, J., Meyer, F., Mahoney, A., Druckenmiller, M. L., Rohith, M., and Kambhamettu, C.: Environmental Security in Arctic Ice-Covered Seas: From Strategy to Tactics of Hazard Identification and Emergency Response, Marine Technology Society Journal, 45, 37–48, https://doi.org/doi:10.4031/MTSJ.45.3.1, 2011.

Feltham, D. L., Untersteiner, N., Wettlaufer, J. S., and Worster, M. G.: Sea ice is a mushy layer, Geophysical Research Letters, 33, https://doi.org/https://doi.org/10.1029/2006GL026290, 2006.

470 Flocco, D., Feltham, D. L., and Turner, A. K.: Incorporation of a physically based melt pond scheme into the sea ice component of a climate model, Journal of Geophysical Research: Oceans, 115, https://doi.org/https://doi.org/10.1029/2009JC005568, 2010.

Galley, R. J., Else, B. G. T., Howell, S. E. L., Lukovich, J. V., and Barber, D. G.: Landfast Sea Ice Conditions in the Canadian Arctic : 1983 – 2009, Arctic, 65, 133–144, 2012.

Gearheard, S., Matumeak, W., Angutikjuaq, I., Maslanik, J., Huntington, H. P., Leavitt, J., Kagak, D. M., Tigullaraq, G., and Barry, 475 R. G.: "It's Not that Simple": A Collaborative Comparison of Sea Ice Environments, Their Uses, Observed Changes, and Adaptations in Barrow, Alaska, USA, and Clyde River, Nunavut, Canada, AMBIO: A Journal of the Human Environment, 35, 203 – 211, https://doi.org/10.1579/0044-7447(2006)35[203:INTSAC]2.0.CO;2, 2006.

Granskog, M. A., Rösel, A., Dodd, P. A., Divine, D., Gerland, S., Martma, T., and Leng, M. J.: Snow contribution to first-year and second-year Arctic sea ice mass balance north of Svalbard, Journal of Geophysical Research: Oceans, 122, 2539–2549, 480 https://doi.org/https://doi.org/10.1002/2016JC012398, 2017.

Gultepe, I., Isaac, G. A., Williams, A., Marcotte, D., and Strawbridge, K. B.: Turbulent heat fluxes over leads and polynyas, and their effects on arctic clouds during FIRE.ACE: Aircraft observations for April 1998, Atmosphere-Ocean, 41, 15–34, https://doi.org/10.3137/ao.410102, 2003.

Hibler, W. D.: A dynamic thermodynamic sea ice model, Journal of Physical Oceanography, 9, 815–846, 1979.

485 Holland, M. M., Bailey, D. A., Briegleb, B. P., Light, B., and Hunke, E.: Improved Sea Ice Shortwave Radiation Physics in CCSM4: The Impact of Melt Ponds and Aerosols on Arctic Sea Ice, Journal of Climate, 25, 1413 – 1430, https://doi.org/10.1175/JCLI-D-11-00078.1, 2012.

Howell, S. E. L., Wohlleben, T., Dabboor, M., Derksen, C., Komarov, A., and Pizzolato, L.: Recent changes in the exchange of sea ice between the Arctic Ocean and the Canadian Arctic Archipelago, Journal of Geophysical Research: Oceans, 118, 3595–3607, 490 https://doi.org/https://doi.org/10.1002/jgrc.20265, 2013.

Hunke, E. C. and Dukowicz, J. K.: An Elastic–Viscous–Plastic Model for Sea Ice Dynamics, Journal of Physical Oceanography, 27, 1849 – 1867, https://doi.org/10.1175/1520-0485(1997)027<1849:AEVPMF>2.0.CO;2, 1997.

Hunke, E. C., Hebert, D. A., and Lecomte, O.: Level-ice melt ponds in the Los Alamos sea ice model, CICE, Ocean Modelling, 71, 26–42, https://doi.org/https://doi.org/10.1016/j.ocemod.2012.11.008, arctic Ocean, 2013.

495 Huwald, H., Tremblay, L.-B., and Blatter, H.: A multilayer sigma-coordinate thermodynamic sea ice model: Validation against Surface Heat Budget of the Arctic Ocean (SHEBA)/Sea Ice Model Intercomparison Project Part 2 (SIMIP2) data, Journal of Geophysical Research: Oceans, 110, https://doi.org/https://doi.org/10.1029/2004JC002328, 2005.

Jackson, K., Wilkinson, J., Maksym, T., Meldrum, D., Beckers, J., Haas, C., and Mackenzie, D.: A Novel and Low-Cost Sea Ice Mass Balance Buoy, Journal of Atmospheric and Oceanic Technology, 30, 2676 – 2688, https://doi.org/10.1175/JTECH-D-13-00058.1, 2013.

500 King, J., Howell, S., Brady, M., Toose, P., Derksen, C., Haas, C., and Beckers, J.: Local-scale variability of snow density on Arctic sea ice, The Cryosphere, 14, 4323–4339, https://doi.org/10.5194/tc-14-4323-2020, 2020.

Kirillov, S., Babb, D. G., Komarov, A. S., Dmitrenko, I., Ehn, J. K., Worden, E., Candlish, L., Rysgaard, S., and Barber, D. G.: On the Physical Settings of Ice Bridge Formation in Nares Strait, Journal of Geophysical Research: Oceans, 126, e2021JC017 331, https://doi.org/https://doi.org/10.1029/2021JC017331, e2021JC017331 2021JC017331, 2021.

505 Kwok, R.: Exchange of sea ice between the Arctic Ocean and the Canadian Arctic Archipelago, Geophysical Research Letters, 33, L16 501, https://doi.org/https://doi.org/10.1029/2006GL027094, 2006.

Lemieux, J.-F., Tremblay, L. B., Dupont, F., Plante, M., Smith, G. C., and Dumont, D.: A basal stress parameterization for modeling landfast ice, Journal of Geophysical Research: Oceans, 120, 3157–3173, https://doi.org/https://doi.org/10.1002/2014JC010678, 2015.

Lemieux, J.-F., Dupont, F., Blain, P., Roy, F., Smith, G. C., and Flato, G. M.: Improving the simulation of landfast ice by com-
510 bining tensile strength and a parameterization for grounded ridges, Journal of Geophysical Research: Oceans, 121, 7354–7368, https://doi.org/https://doi.org/10.1002/2016JC012006, 2016.

Liao, Z., Cheng, B., Zhao, J., Vihma, T., Jackson, K., Yang, Q., Yang, Y., Zhang, L., Li, Z., Qiu, Y., and Cheng, X.: Snow depth and ice thickness derived from SIMBA ice mass balance buoy data using an automated algorithm, International Journal of Digital Earth, 12, 962–979, https://doi.org/10.1080/17538947.2018.1545877, 2019.

515 Liu, Y., Losch, M., Hutter, N., and Mu, L.: A New Parameterization of Coastal Drag to Simulate Landfast Ice in Deep Marginal Seas in the Arctic, Journal of Geophysical Research: Oceans, 127, e2022JC018 413, https://doi.org/https://doi.org/10.1029/2022JC018413, e2022JC018413 2022JC018413, 2022.

Lüpkes, C., Vihma, T., Birnbaum, G., and Wacker, U.: Influence of leads in sea ice on the temperature of the atmospheric boundary layer during polar night, Geophysical Research Letters, 35, L03 805, https://doi.org/10.1029/2007GL032461, 2008.

520 Maksym, T. and Jeffries, M. O.: A one-dimensional percolation model of flooding and snow ice formation on Antarctic sea ice, Journal of Geophysical Research: Oceans, 105, 26 313–26 331, https://doi.org/https://doi.org/10.1029/2000JC900130, 2000.

Maykut, G. A. and Untersteiner, N.: Some results from a time-dependent thermodynamic model of sea ice, Journal of Geophysical Research (1896-1977), 76, 1550–1575, https://doi.org/https://doi.org/10.1029/JC076i006p01550, 1971.

Melling, H.: Sea ice of the northern Canadian Arctic Archipelago, Journal of Geophysical Research: Oceans, 107, 2–1–2–21,
525 https://doi.org/https://doi.org/10.1029/2001JC001102, 2002.

Melling, H., Gratton, Y., and Ingram, G.: Ocean circulation within the North Water polynya of Baffin Bay, Atmosphere-Ocean, 39, 301–325, https://doi.org/10.1080/07055900.2001.9649683, 2001.

Merkouriadi, I., Liston, G. E., Graham, R. M., and Granskog, M. A.: Quantifying the Potential for Snow-Ice Formation in the Arc-
tic Ocean, Geophysical Research Letters, 47, e2019GL085 020, https://doi.org/https://doi.org/10.1029/2019GL085020, e2019GL085020
530 2019GL085020, 2020.

Notz, D. and Worster, M. G.: Desalination processes of sea ice revisited, Journal of Geophysical Research: Oceans, 114, https://doi.org/https://doi.org/10.1029/2008JC004885, 2009.

Planck, C. J., Whitlock, J., Polashenski, C., and Perovich, D.: The evolution of the seasonal ice mass balance buoy, Cold Regions Science and Technology, 165, 102 792, https://doi.org/https://doi.org/10.1016/j.coldregions.2019.102792, 2019.

535 Plante, M., Tremblay, B., Losch, M., and Lemieux, J.-F.: Landfast sea ice material properties derived from ice bridge simulations using the Maxwell elasto-brittle rheology, The Cryosphere, 14, 2137–2157, https://doi.org/10.5194/tc-14-2137-2020, 2020.

Pringle, D. J., Eicken, H., Trodahl, H. J., and Backstrom, L. G. E.: Thermal conductivity of landfast Antarctic and Arctic sea ice, Journal of Geophysical Research: Oceans, 112, https://doi.org/https://doi.org/10.1029/2006JC003641, 2007.

Provost, C., Sennéchael, N., Miguet, J., Itkin, P., Rösel, A., Koenig, Z., Villacieros-Robineau, N., and Granskog, M. A.: Observations of
540 flooding and snow-ice formation in a thinner Arctic sea-ice regime during the N-ICE2015 campaign: Influence of basal ice melt and storms, Journal of Geophysical Research: Oceans, 122, 7115–7134, https://doi.org/https://doi.org/10.1002/2016JC012011, 2017.

Raddatz, R. L., Asplin, M. G., Candlish, L., and Barber, D. G.: General Characteristics of the Atmospheric Boundary Layer Over a Flaw
Lead Polynya Region in Winter and Spring, Boundary-Layer Meteorology, 138, 321–335, https://doi.org/10.1007/s10546-010-9557-1,
2011.

545 Rampal, P., Bouillon, S., Ólason, E., and Morlighem, M.: neXtSIM: a new Lagrangian sea ice model, The Cryosphere, 10, 1055–1073,
https://doi.org/10.5194/tc-10-1055-2016, 2016.

Richter-Menge, J. A., Perovich, D. K., Elder, B. C., Claffey, K., Rigor, I., and Ortmeyer, M.: Ice mass-balance buoys: a
tool for measuring and attributing changes in the thickness of the Arctic sea-ice cover, Annals of Glaciology, 44, 205–210,
https://doi.org/10.3189/172756406781811727, 2006.

550 Rösel, A., Itkin, P., King, J., Divine, D., Wang, C., Granskog, M. A., Krumpen, T., and Gerland, S.: Thin Sea Ice, Thick Snow, and
Widespread Negative Freeboard Observed During N-ICE2015 North of Svalbard, Journal of Geophysical Research: Oceans, 123, 1156–
1176, https://doi.org/https://doi.org/10.1002/2017JC012865, 2018.

Semtner, A. J.: A Model for the Thermodynamic Growth of Sea Ice in Numerical Investigations of Climate, Journal of Physical Oceanogra-
phy, 6, 379 – 389, https://doi.org/10.1175/1520-0485(1976)006<0379:AMFTTG>2.0.CO;2, 1976.

555 Smith, G. C., Bélanger, J.-M., Roy, F., Pellerin, P., Ritchie, H., Onu, K., Roch, M., Zadra, A., Colan, D. S., Winter, B., Fontecilla, J.-S., and
Deacu, D.: Impact of Coupling with an Ice–Ocean Model on Global Medium-Range NWP Forecast Skill, Monthly Weather Review, 146,
1157 – 1180, https://doi.org/10.1175/MWR-D-17-0157.1, 2018.

Smith, G. C., Liu, Y., Benkiran, M., Chikhar, K., Surcel Colan, D., Gauthier, A.-A., Testut, C.-E., Dupont, F., Lei, J., Roy, F., Lemieux, J.-F.,
and Davidson, F.: The Regional Ice Ocean Prediction System v2: a pan-Canadian ocean analysis system using an online tidal harmonic
560 analysis, Geoscientific Model Development, 14, 1445–1467, https://doi.org/10.5194/gmd-14-1445-2021, 2021.

Stirling, I.: The Biological Importance of Polynyas in the Canadian Arctic, Arctic, 33, 303–315, 1980.

Stirling, I.: The importance of polynyas, ice edges, and leads to marine mammals and birds, Journal of Marine Systems, 10, 9–21,
https://doi.org/https://doi.org/10.1016/S0924-7963(96)00054-1, 1997.

Tremblay, J.-E., Gratton, Y., Carmack, E. C., Payne, C. D., and Price, N. M.: Impact of the large-scale Arctic circulation and
565 the North Water Polynya on nutrient inventories in Baffin Bay, Journal of Geophysical Research: Oceans, 107, 26–1–26–14,
https://doi.org/https://doi.org/10.1029/2000JC000595, 2002.

Tremblay, L.-B. and Mysak, L. A.: Modeling Sea Ice as a Granular Material, Including the Dilatancy Effect, Journal of Physical Oceanogra-
phy, 27, 2342 – 2360, https://doi.org/10.1175/1520-0485(1997)027<2342:MSIAAG>2.0.CO;2, 1997.

Turner, A. K. and Hunke, E. C.: Impacts of a mushy-layer thermodynamic approach in global sea-ice simulations using the CICE sea-ice
570 model, Journal of Geophysical Research: Oceans, 120, 1253–1275, https://doi.org/https://doi.org/10.1002/2014JC010358, 2015.

Turner, A. K., Hunke, E. C., and Bitz, C. M.: Two modes of sea-ice gravity drainage: A parameterization for large-scale modeling, Journal
of Geophysical Research: Oceans, 118, 2279–2294, https://doi.org/https://doi.org/10.1002/jgrc.20171, 2013.

Ungermann, M., Tremblay, L. B., Martin, T., and Losch, M.: Impact of the ice strength formulation on the perfor-
mance of a sea ice thickness distribution model in the Arctic, Journal of Geophysical Research: Oceans, 122, 2090–2107,
575 https://doi.org/https://doi.org/10.1002/2016JC012128, 2017.

West, A., Collins, M., and Blockley, E.: Using Arctic ice mass balance buoys for evaluation of modelled ice energy fluxes, Geoscientific
Model Development, 13, 4845–4868, https://doi.org/10.5194/gmd-13-4845-2020, 2020.

Wilchinsky, A. V. and Feltham, D. L.: A continuum anisotropic model of sea-ice dynamics, Proceedings of the Royal Society of London.
Series A: Mathematical, Physical and Engineering Sciences, 460, 2105–2140, https://doi.org/10.1098/rspa.2004.1282, 2004.

580 Wongpan, P., Hughes, K. G., Langhorne, P. J., and Smith, I. J.: Brine Convection, Temperature Fluctuations, and Permeability in Winter Antarctic Land-Fast Sea Ice, Journal of Geophysical Research: Oceans, 123, 216–230, https://doi.org/https://doi.org/10.1002/2017JC012999, 2018.

Zuo, G., Dou, Y., and Lei, R.: Discrimination Algorithm and Procedure of Snow Depth and Sea Ice Thickness Determination Using Measurements of the Vertical Ice Temperature Profile by the Ice-Tethered Buoys, Sensors, 18, https://doi.org/10.3390/s18124162, 2018.
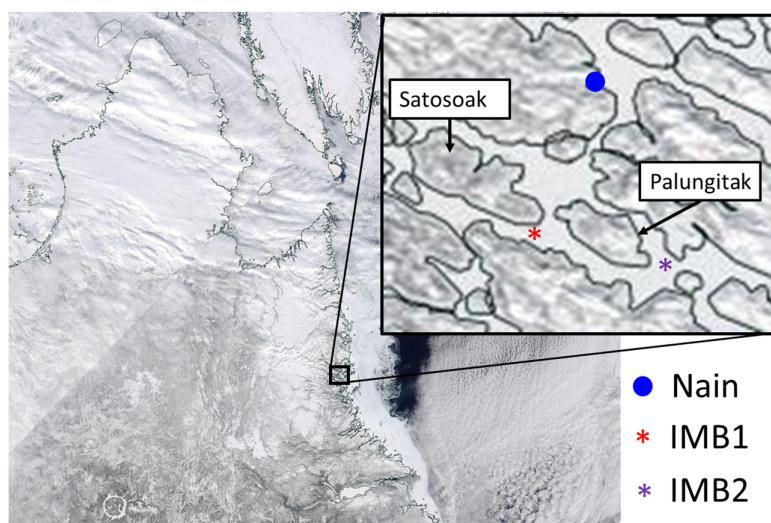
Figure 1. Location of the two IMB buoys deployed in the landfast ice close to Nain, Labrador. Images are corrected reflectance imagery from MODIS worldview (https://earthdata.nasa.gov/labs/worldview/).
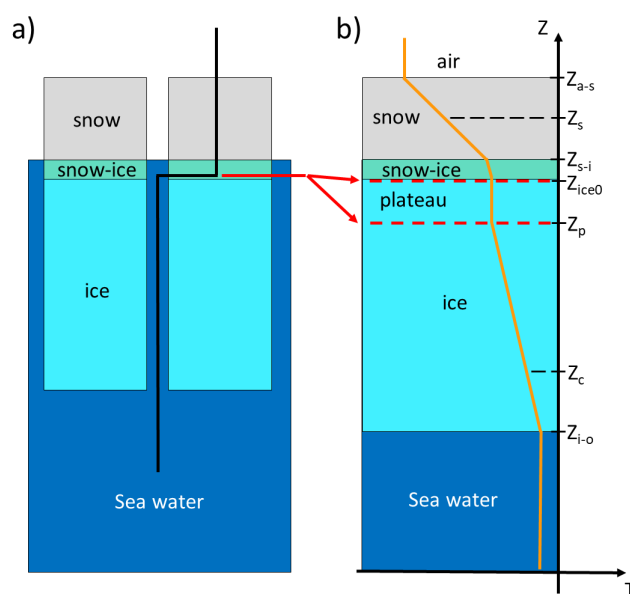
Figure 2. Schematics of the deployed SAMS IMB buoy thermistor strings through the snow, snow-ice and sea ice layers (a) and the vertical temperature profiles they measure (b) with the sensor positions used in the surface retrieval algorithm. Note the section of the thermistor string (thermistor plateau, red lines) laid flat on the bare ice surface at deployment but later embedded within the ice layer after flooding.
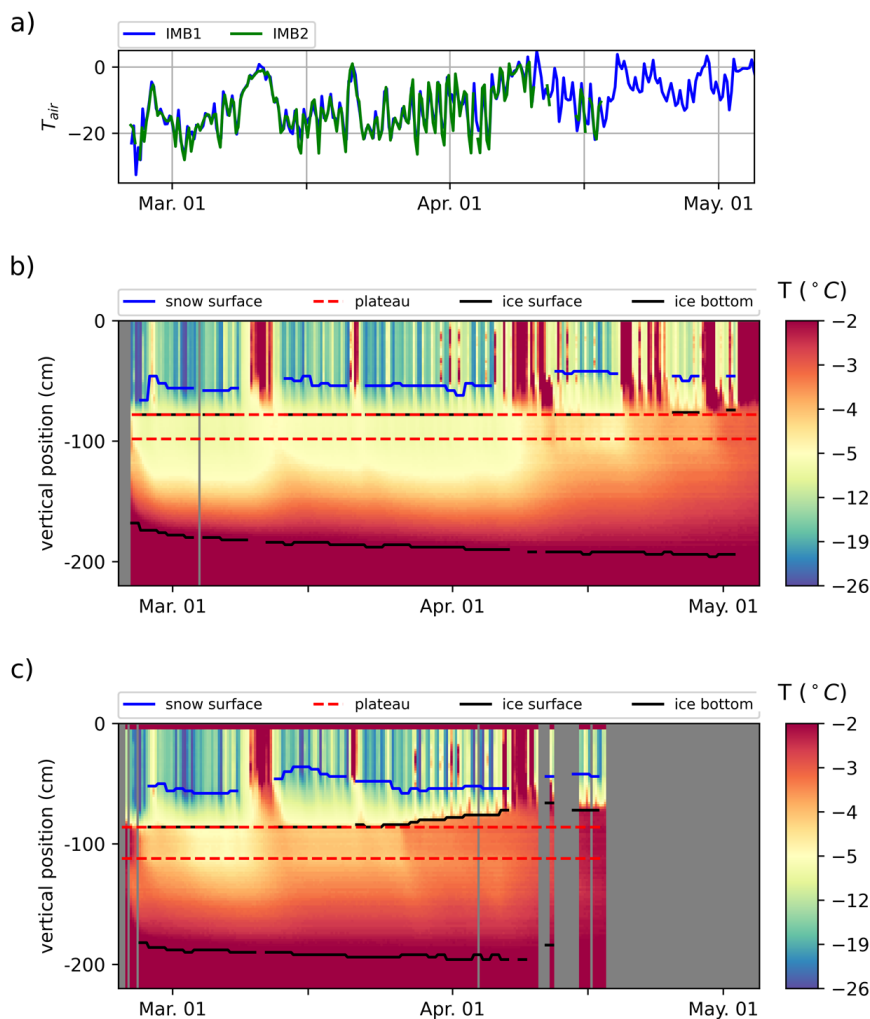
Figure 3. Time series of the temperatures recorded by the IMB buoys and interfaces detected by the automated algrithm. a) Air temperatures recorded by the IMB1 (blue) and IMB2 (green) buoys. b) Temperatures along the IMB1 thermistor string (color) with the detected material interfaces (air-snow interface in blue, ice top and bottom in black and thermistor string plateau in red). c) Same as (b) but for the IMB2 buoy.
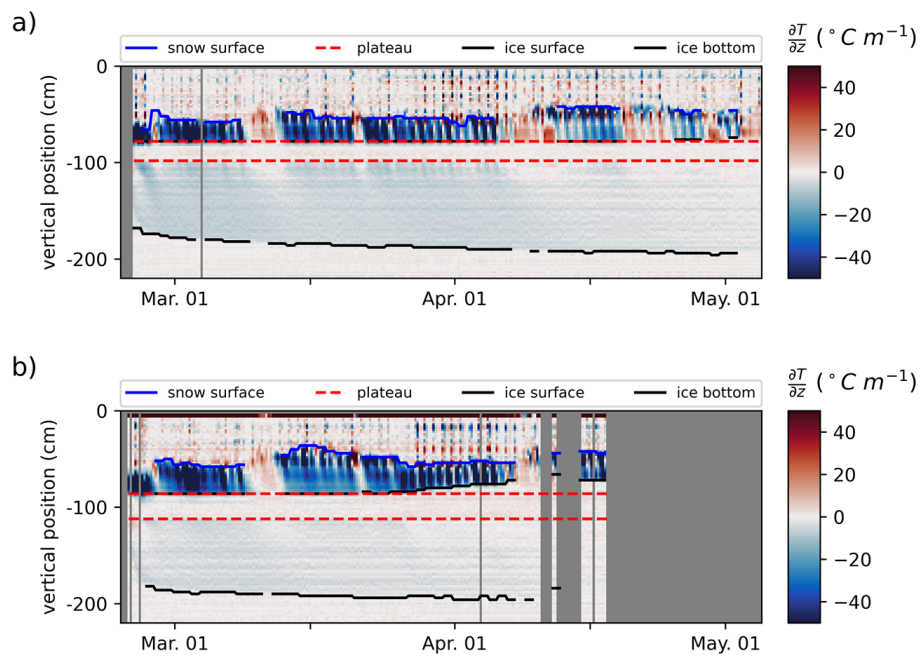
Figure 4. Vertical temperature gradients (color) along the IMB1 (a) and IMB2 (b) thermistor strings. Colored lines indicate the detected material interfaces (air-snow interface in blue, ice top and bottom in black and thermistor string plateau in red).
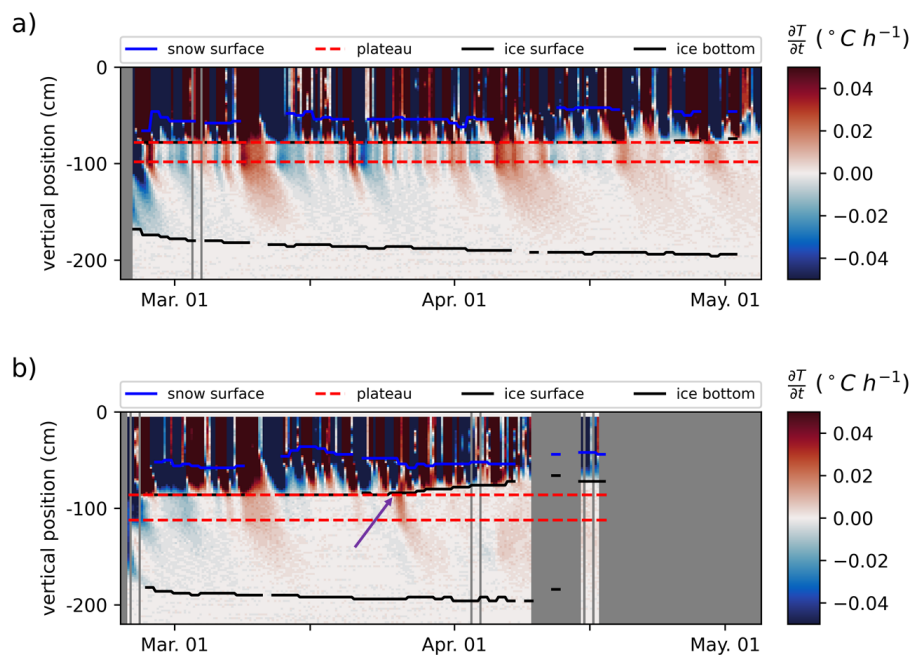
Figure 5. Rates of temperature changes (color) at each sensors of the IMB1 (a) and IMB2 (b) thermistor strings over the observation records. Colored lines indicate the detected material interfaces (air-snow interface in blue, ice top and bottom in black and thermistor string plateau in red).
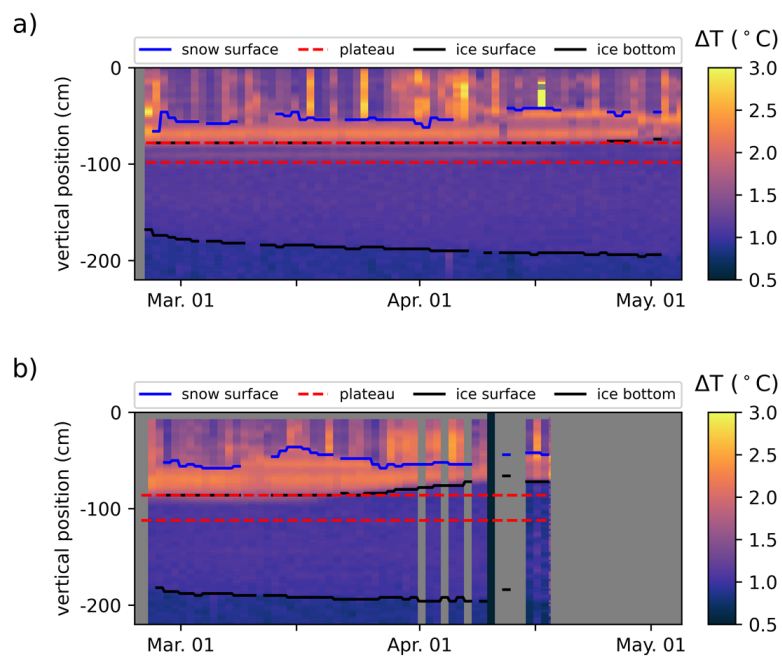
Figure 6. Change in temperature (color) at each sensor as measured after 2 min of heating during the daily heating cycles, for IMB1 (a) and IMB2 (b). The colored lines indicate the material interfaces detected using the automated algorithm: the air-snow interface (blue), the ice top and bottom interfaces (black) and the thermistor string plateau (dashed red).
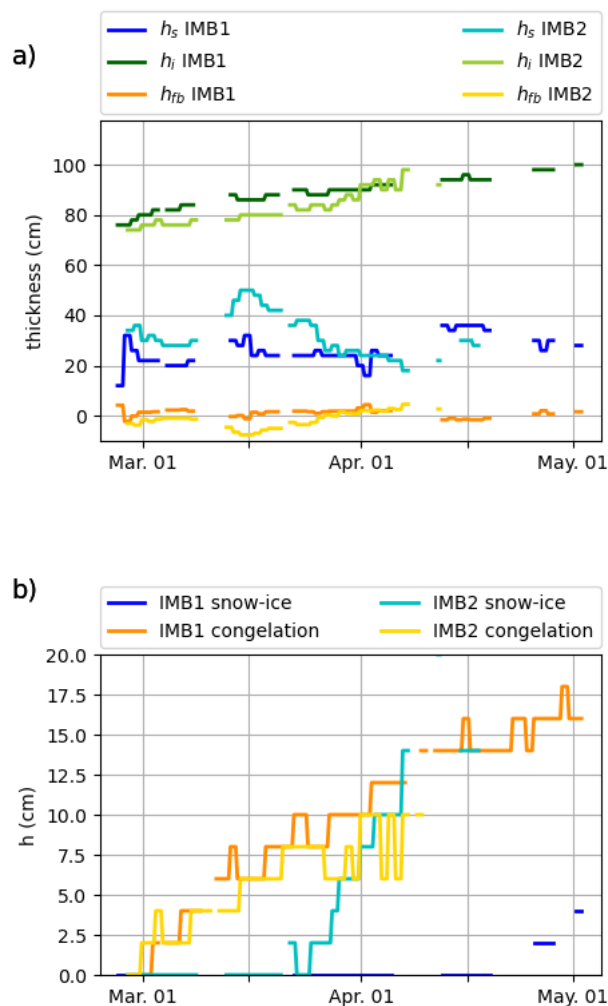
Figure 7. a) Snow (blue lines), ice (green lines) and freeboard (orange lines) thicknesses from the IMB observations. a) Contribution of snow-ice (blue lines) and congelation (orange lines) to the ice mass balance inferred from the IMB observations.
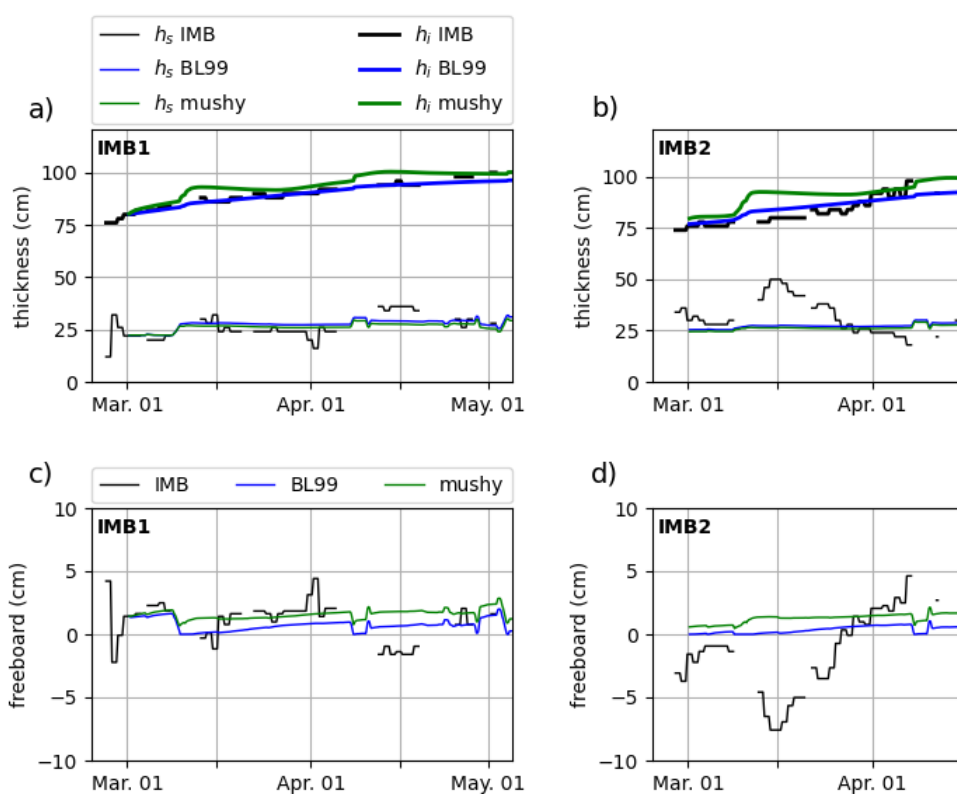
Figure 8. Snow depth (a, b, thin lines), ice thickness (a, b, thick lines) and the computed freeboard values (c,d) from the IMB observations (black), the BL99 simulations (blue) and the mushy layer simulations (green), for the two IMB buoy cases (a,c: IMB1, c,d: IMB2).
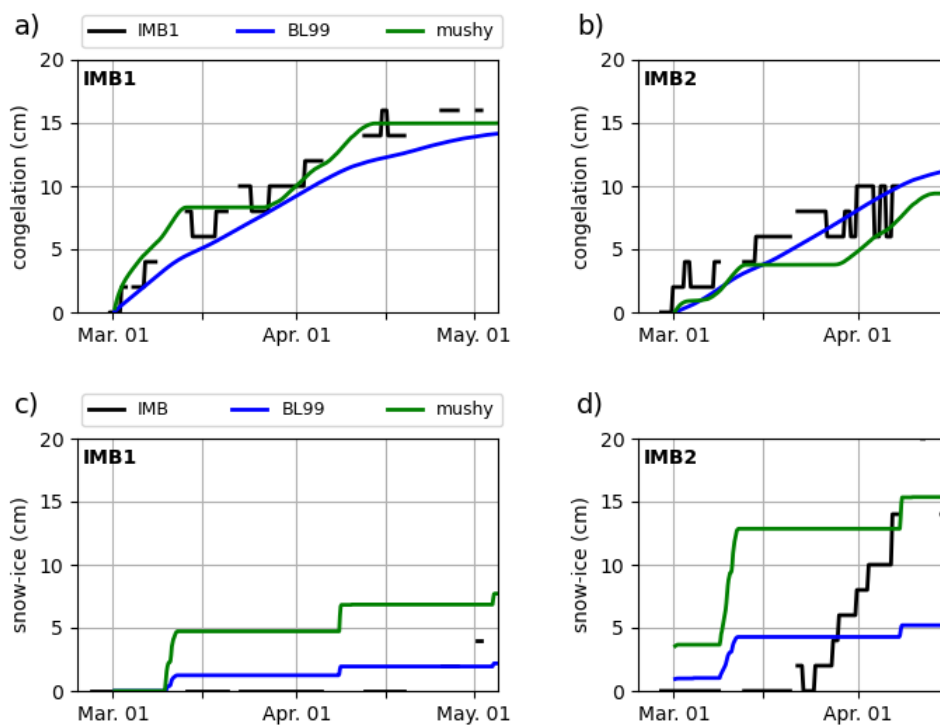
Figure 9. Cumulative ice congelation (a, b) and snow ice formation (c, d) from the IMB observations (black), the BL99 simulations (blue) and the mushy layer simulations (green), for the two IMB buoy cases (a,c: IMB1, c,d: IMB2).
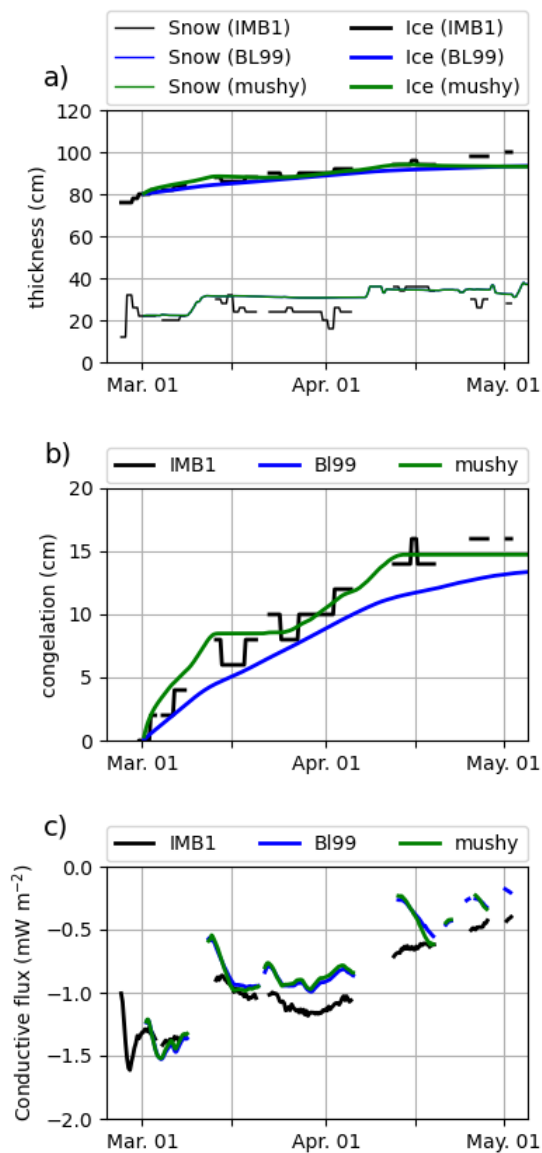
Figure 10. Ice mass balance from the IMB1 observations (black), the BL99 simulations (blue) and the mushy layer simulations (green), when simulations are run without the snow-ice parameterizations. a) Snow depth (thin lines) and ice thickness (thick lines), b) cumulative ice congelation and c) measured conductive fluxes.
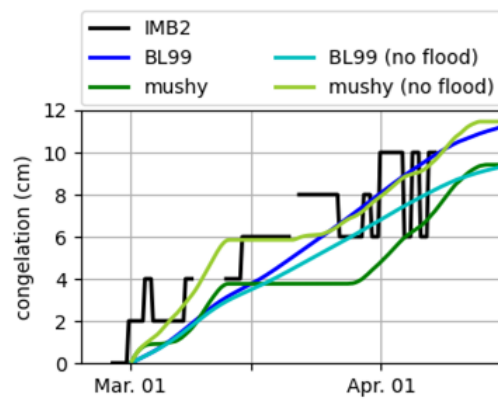
Figure 11. Impact of the snow-ice parameterizations on the ice congelation in IMB2 simulations. Lines indicate the cumulative congelation from the IMB observations (black), the BL99 simulation (blue), the BL99 simulation without flooding (cyan), the mushy layer simulation (green) and the mushy layer simulation without flooding (olive).
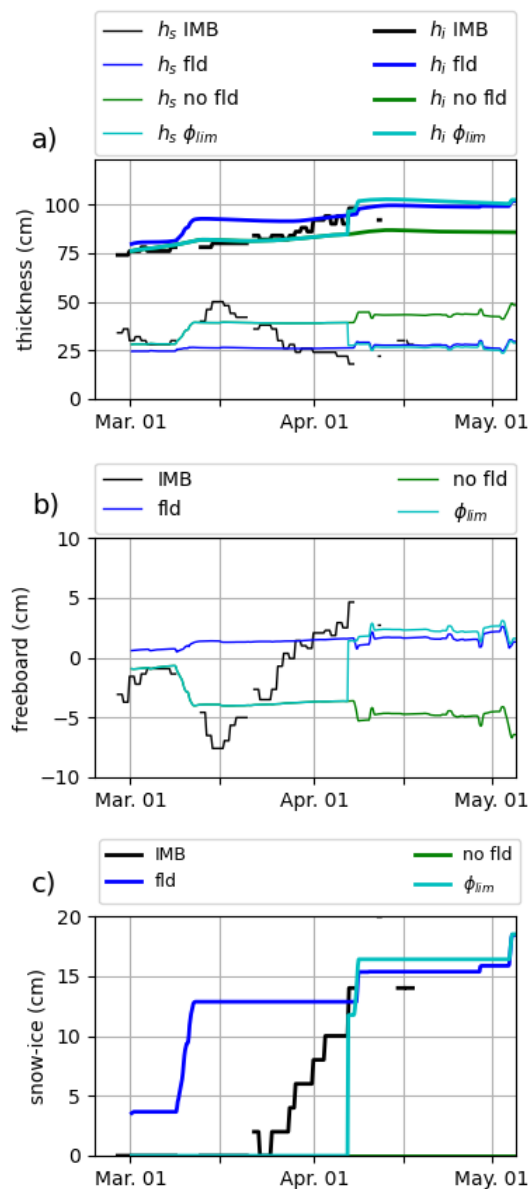
Figure 12. Snow depth (a, thin lines), ice thickness (a, thick lines), freeboard values (b) and cumulative snow-ice formation (c) from the IMB2 observations (black) and in simulation with different snow-ice parameterizations: the mushy layer parameterizations (blue), the mushy layer without flooding (green) and the mushy layer parameterization with an added liquid fraction threshold (ϕ_{min}=0.06) for permeability (cyan).